Single solitons and intermode breathing solitons in MgF_2 microresonators

Alioune Niang,* Logan Courtright, Gary Carter, and Curtis R. Menyuk
Department of Computer Science and Electrical Engineering, University of Maryland, Baltimore County, Baltimore, Maryland, USA

(Received 15 May 2025; accepted 1 July 2025; published 30 July 2025)

Intermode breathers can be triggered by the avoided mode crossings in microresonators. Here, we numerically and experimentally explore the breather and single soliton regimes as the pump-power and pump-cavity detuning vary. Below a pump-power threshold, a single soliton regime is obtained within a detuning range. Above this threshold, an intermode breather section emerges, resulting in a soliton-breather-soliton pattern in which the system transits from a stable soliton to a breathing soliton and back to a stable soliton as the detuning increases.

DOI: 10.1103/bkzf-65qy

I. INTRODUCTION

During the past 15 years, Kerr optical frequency combs that are generated by microresonators have been the subject of strong interest due to their many potential applications [1–4] and have been the subject of a large number of theoretical and experimental studies, including [5–12]. To generate frequency combs in a microresonator, the usual method is to couple a continuous-wave (CW) laser into a microresonator with sufficiently high Q so that intracavity energy is high enough for the Kerr effect to cascade energy into nonresonant longitudinal modes whose angular group velocities become locked [13,14], which can then create a number of different comb states [5,15], including primary combs (Turing rolls), secondary combs (modulation-instability, MI) or soliton combs (dissipative Kerr solitons).

Careful management of the optical pump power and frequency detuning of the pump laser frequency from the resonator mode frequency is crucial for access to the comb states. In Refs. [16–20], the authors studied theoretically the existence and stability of different comb states as a function of the pump power and the cavity detuning. In [19] Lucas *et al*. experimentally mapped the stability chart of solitons in the pump-power detuning space and compared it with theoretical predictions.

Soliton states are useful in practice because they generate frequency combs with a constant free spectral range (FSR), which in turn generate strong radio-frequency tones at frequencies equal to the FSR and its harmonics after detection in a photodiode. Single solitons [15,21], double solitons [22], breathing solitons [23–25], and soliton crystals [12,20,26–29] have all been observed in microresonators and testify to the rich collection of optical wave forms that can be created in these devices. However, experimentally accessing particular wave forms—and in particular, single solitons—can be an experimental challenge due to thermal effects inside the microresonator. Several passive methods have been developed to stabilize the temperature inside the resonator so that soliton combs can be created and maintained [5–12,22,29–32].

On the other hand, the interaction between transverse modes due to an avoided crossing can lead to a deterministic generation of a soliton or a soliton crystal [15,20–22,29,33].

Recently, Guo *et al*. demonstrated a novel type of breathing soliton triggered by avoided mode crossings [34] in a microresonator. This new type of breathing soliton that they named an "intermode breather soliton" occurs due to a periodic energy exchange between the soliton and another transverse mode family [34]. Moreover, as opposed to the classical or intrinsic breather, the intermode breather only appears in the same detuning range where a stable soliton is expected. The intermode breather was first experimentally observed by Lucas *et al.* [35] before being investigated in more detail in Ref. [34]. In both works, the authors studied its detuning dependence without exploring the effects of varying the pump power.

In this work we experimentally explore soliton dynamics by studying both the pump power and detuning dependencies of the single soliton and intermode breather in a crystalline magnesium fluoride (MgF_2) microresonator. We map the occurrence of both the single soliton and intermode breather regimes in the pump power–detuning parameter space. As a function of detuning, our observations show that below a threshold pump power stable breather solutions do not exist. However, when the pump power is above this threshold, a stable soliton can transition to an intermode breather and then transition back to the soliton state, referred to as a soliton-breather-soliton pattern, when the detuning is changed.

To perform this experiment, we adapt the approach described by Cole *et al.* [32], where a backward-propagating wave is used to both stabilize the temperature in the microresonator and to control the pump-cavity detuning.

We next numerically investigate the soliton and intermode breather dynamics using the Lugiato-Lefever equation (LLE) with an avoided crossing. The numerical results are consistent

*Contact author: aniang1@umbc.edu

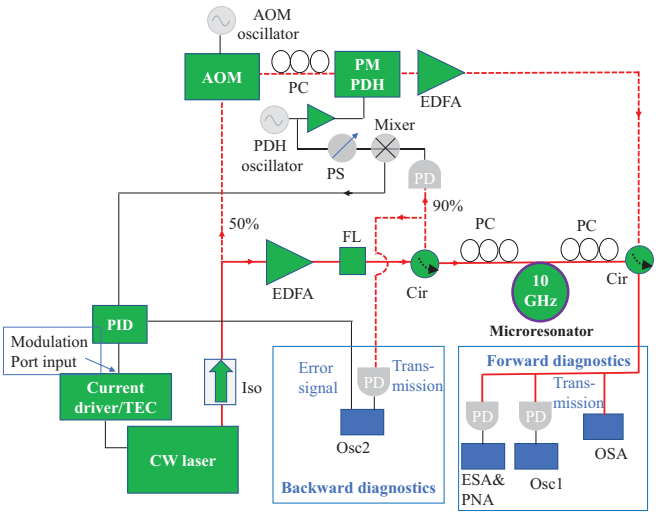

FIG. 1. Schematic of the experimental setup. A continuous-wave (CW) laser is both forward (red solid) and backward (red dash) coupled into a microresonator.

with our experimental observations. Notably, the numerical model we use is based on the "standard" version of the LLE [27], which does not allow for energy exchange between transverse mode families. As such, we show numerically that there does not need to be energy exchange of this sort for intermode breathers to appear.

More recently, a similar result (soliton-breather-soliton) was numerically reported by Chen *et al*. [36] in the presence of loss modulation in the resonator. However, Chen *et al*. focused instead on the intrinsic breather rather than on this transition.

II. EXPERIMENTAL RESULTS: SOLITONS AND INTERMODE BREATHER GENERATION

To experimentally generate soliton combs, we adapt the approach described by Cole *et al*. [32]. We show a schematic illustration of the setup in Fig. 1. It is an all-fiber coupled configuration. A CW laser (at 1550 nm) is split off and 50% is directly amplified by an erbium-doped fiber amplifier (EDFA), after which it is launched into a MgF_2 whispering-gallery-mode microresonator with a free spectral range of around 10 GHz. This forward-propagating optical path is used to generate soliton combs. In addition, we use a filter (FL) to suppress the amplified spontaneous emission (ASE) noise. The second 50% of the laser light goes to an acousto-optic modulator (AOM) that upshifts the pump frequency by 40 MHz. The light is then phase modulated by a PM (phase modulation) PDH (Pound-Drever-Hall) modulator that has a variable frequency. This phase-modulated signal then propagates in the backward direction through the resonator after being amplified by an EDFA. This backward-propagating signal stabilizes the temperature of the microresonator so that we can obtain stable solitons in the microresonator [32]. We then mix the backward-propagating signal after the photodetector with the output of the PDH oscillator to produce a low-frequency voltage signal that is sent to a proportional-integral-derivative (PID) controller in order to lock the redshifted sideband to the resonance. By manually varying the PDH oscillator frequency, we can control the pump-cavity detuning, $\delta = \nu_0 - \nu_{\text{pump}}$, where ν_0 and ν_{pump} are the resonance frequency and the pump laser frequency, respectively, of the forward carrier from the cavity resonance. The difference between the AOM (f_{AOM}) and the PDH (f_{PDH}) frequencies equals pump-cavity detuning ($\nu_0 - \nu_{\text{pump}} = f_{\text{AOM}} - f_{\text{PDH}}$) [32]. The output of both forward- and backward-propagating signals are sent to an OSA (optical spectrum analyzer), ESA (electrical spectrum analyzer), PNA (phase noise analyzer), and an oscilloscope for characterization. For the frequency and phase noise measurements, the forward output signal is filtered by fiber Bragg grating (FBG) filters, not shown in Fig. 1, in order to suppress the pump light and then amplified by an EDFA before entering into a photodetector (PD). We show the optical fibers in red and the electrical cables in black.

By controlling the forward and backward pump power and the detuning frequency, we can deterministically obtain soliton combs when the laser is locked using the PDH method, as described in the previous paragraph. In order to compensate for thermal effects that can destabilize the soliton, the backward power was fixed at 40 mW during the experiments. Figure 2(a) shows the optical spectrum of the single soliton that was generated with a forward pump power $P = 145$ mW and with a detuning frequency $\delta = 1.5$ MHz. The spike at 1552.5 nm is approximately 10 dB stronger than the background hyperbolic-secant spectrum and is a characteristic of an avoided crossing, indicating that two transverse modes are interacting [34]. While we used the approach described in Ref. [37] to measure the integrated dispersion (D_{int}) of the microresonator around 1550 nm, we were unable to experimentally accurately measure the avoided crossing strength and location due to the noise present in our dispersion measurements, which greatly exceeded the expected strength value of the mode interaction.

In Fig. 2(b) we present the rf spectrum that is generated by the beat between the soliton comb lines and is centered at around 9.9136 GHz, which equals the repetition rate (f_{rep}) of the soliton in microresonator. The two sidebands (smaller lines) are displaced from the repetition rate frequency by 1.5 MHz, which corresponds to the detuning frequency. Next, the detuning is held at 1.5 MHz and the pump power is increased. Above $P \approx 160$ mW, two additional sidebands appear in the electric spectrum analyzer, indicating that the system has entered the soliton breather regime in which the soliton amplitude is oscillating [23,24,35]. Figure 2(d) shows an example where the pump power is 190 mW. Sidebands are visible at around ± 1.38 MHz due to the breathing frequency, which is lower than the repetition rate of the soliton [23,24,35]. This intermode breathing appears due to the avoided mode crossings and appears in the region of the pump-power detuning parameter space where a single soliton is stable. Our observation is in agreement with the reported results in Ref. [35], where the detuning dependence was investigated. The corresponding optical spectrum is presented in Fig. 2(c). Furthermore, we measure the phase noise in both the soliton and breathing soliton regimes. Figure 3 displays the single-sideband (SSB) phase noise level of both single and breathing solitons. The breathing regime (red) shows an increased phase noise relative to the single soliton (blue). Thus,

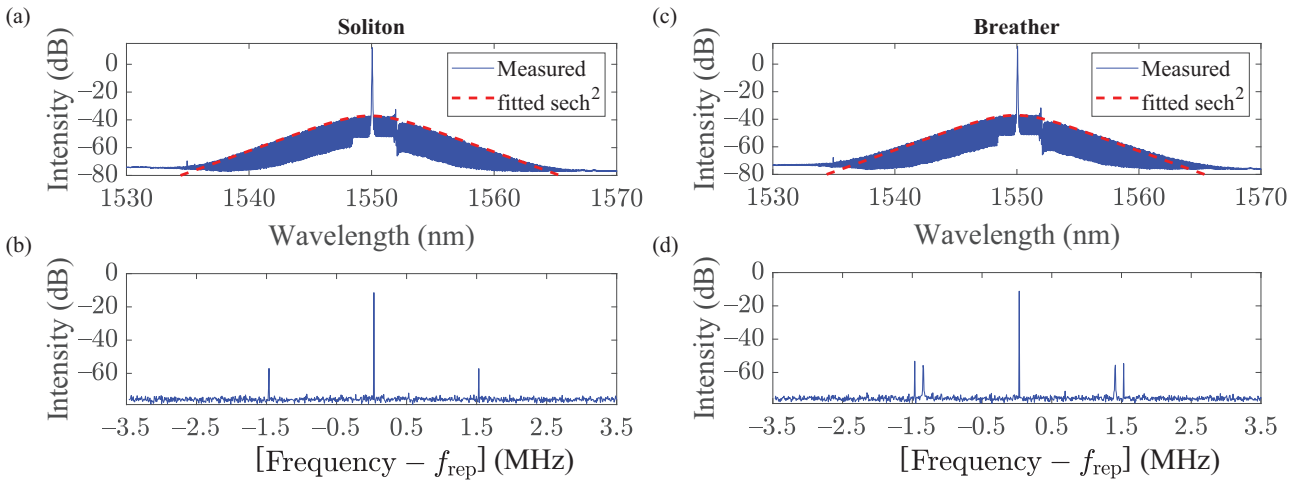

FIG. 2. Single soliton and breathing regimes. (a), (c) Optical spectra for the single soliton and breather soliton, respectively. (b), (d) The corresponding rf spectra centered at $f_{rep} = 9.9136$ GHz.

as expected, breathing degrades the soliton stability [19,35].

In the last series of experiments, we studied the stability of both soliton and breather dynamics in the pump power–detuning parameter space. First, we locked the laser at a fixed detuning with a pump power ≈200 mW, which is the maximum operating power in our system. Next, we fixed the detuning while the forward-propagating pump power was varied until the soliton disappeared. We then reset the detuning to a new value and repeated the measurements. We recorded the pump power and detuning and then mapped the results. The backward pump power was approximately 30 mW.

In Fig. 4 we present the results for the breather and soliton dynamics. In our experiment we found that the soliton existence range is from $\delta \approx 0.8$ MHz to $\delta \approx 2$ MHz. We always obtained a CW regardless of the pump power for a detuning $\delta > 2$ MHz, while we obtained a CW and then MI combs for a detuning $\delta < 0.8$ MHz. When the pump power was above $P \approx 130$ mW, a single soliton or an intermode breathing soliton was observed depending on the detuning. Depending on where in the pump power–detuning parameter space we were located experimentally, we found first a soliton, then a breather, and finally a soliton, yielding a soliton-breather-soliton pattern, which is in good agreement with the Lucas *et al.* [35] predictions. We observe an intermode breathing soliton over a detuning range of ≈0.8 MHz when $P \gtrsim 185$ mW. However, we also observed an intermode breathing soliton over a detuning range of ≈0.7 MHz for 175 mW $\lesssim P \lesssim$ 185 mW and over a detuning range of ≈0.6 MHz for 165 mW $\lesssim P \lesssim$ 175 mW. This result demonstrates that the detuning range of the intermode breathing soliton is dependent on the pump power. Moreover, the soliton-breather-soliton pattern is reversible and reproducible when the detuning is held constant and the pump power is decreased and then increased. The same properties hold when the pump power is held constant and the detuning is increased or decreased.

III. NUMERICAL RESULTS: BOUNDARY TRACKING OF SOLITON STABILITY

To better understand our experimental results, we ran numerical simulations of the Lugiato-Lefever equation using the dynamical methods developed in [27,38,39]. The version of

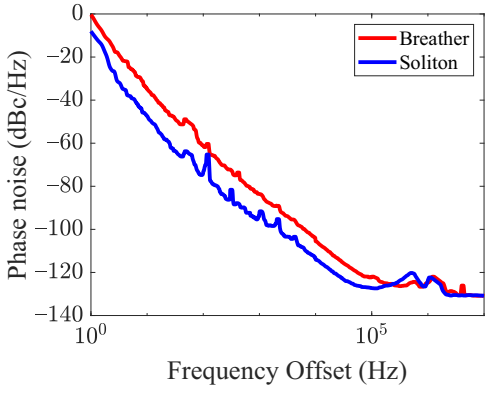

FIG. 3. Single soliton and breathing regimes. Phase noise spectra of the single soliton (blue) and breather soliton (red).

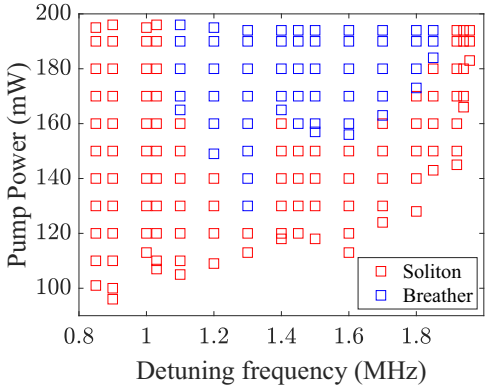

FIG. 4. Experimental measurements. Stable region in the pump power–detuning parameter space for single solitons and breather solitons in detuning and power space.

the LLE we used is written as

$$\frac{\partial\psi}{\partial t} = -i\mathcal{D} * \psi + i|\psi|^2\psi - (i\alpha + 1)\psi + F, \tag{1}$$

where ψ is the normalized field envelope, t is normalized slow time, α is the normalized detuning, F is the normalized pump power, and $\mathcal{D} * \psi = \mathcal{F}t^{-1}[D_{\text{int}}\tilde{\psi}]$, where $\mathcal{F}t^{-1}$ is the inverse Fourier transform, $D_{\text{int}}(\mu)$ is the integrated dispersion, and $\tilde{\psi}$ is the Fourier transform of ψ. In microresonators, the spacing between longitudinal modes is given by the dispersion relation $\omega(\mu) = \omega_0 + D_1\mu + (D_2/2)\mu^2 + (D_3/6)\mu^3 + \cdots$, where μ is the relative mode number with respect to the pumped mode located at $\omega(\mu = 0)$ and $D_1/2\pi$ is the FSR of the cavity at $\omega(\mu = 0)$. $D_{\text{int}}(\mu) = \omega(\mu) - \omega_0 - D_1\mu = (D_2/2)\mu^2 + \cdots$ corresponds to the higher-order dispersion present in the microresonator. For GVD-dominant resonators where D_3 and higher-order terms can be ignored, such as in MgF_2 resonators, $D_{\text{int}} = (D_2/2)\mu^2$ and thus $\mathcal{D} * \psi = (\beta/2)\partial^2\psi/\partial\theta^2$, where θ is the azimuthal coordinate around the microresonator and β is the normalized form of D_2. To account for avoided crossings, we add an extra term $a/(\mu - b)$ to D_{int}, where a is the normalized avoided crossing strength and b is the avoided crossing location in terms of μ, such that $\mathcal{D} * \psi = \mathcal{F}t^{-1}\{[(D_2/2)\mu^2 + a/(\mu - b)]\tilde{\psi}\}$ [33,40]. This formulation of an avoided crossing assumes that the second mode merely perturbs the dispersion of the first and has no further effect, allowing us to consider only one set of longitudinal modes. Additionally, the asymmetry in the dispersion due to the avoided crossing will modify the soliton's angular group velocity, causing the soliton to rotate around the cavity with a new group velocity $v_g = v_{g0} + v_{av}$, where v_g is the group velocity, v_{g0} is the group velocity in the absence of the avoided crossing, and v_{av} is the additional velocity from the avoided crossing. As a result of this change in the group velocity, the solitons in the LLE simulations drift. To obtain a stationary solution, we modified Eq. (1) by adding a drift term. This modified equation can be written as

$$\frac{\partial\psi}{\partial t} = -i\mathcal{D} * \psi + i|\psi|^2\psi - (i\alpha + 1)\psi + F - t_s\frac{\partial\psi}{\partial\theta}, \tag{2}$$

where t_s compensates for the induced drift [38]. We determined t_s in the process of solving for a stationary solution to Eq. (2), as described by Wang *et al.* [38].

We begin our study of the system stability by linearizing the LLE around the real and imaginary parts of a stable stationary solution such that

$$\begin{aligned}\psi_r &= \psi_{r0} + \Delta\psi_r,\\ \psi_i &= \psi_{i0} + \Delta\psi_i,\end{aligned} \tag{3}$$

where ψ_r and ψ_i are real and imaginary parts of ψ, respectively. The stationary solution $\psi_0 = \psi_{r0} + i\psi_{i0}$ is found using a variant of the Newton-Raphson method applied to Eq. (2), with $\partial\psi/\partial t$ set to zero while solving for t_s simultaneously. From there, we substitute Eq. (3) into Eq. (2) and obtain an eigenvalue equation for the perturbations,

$$\frac{\partial\Delta\boldsymbol{\Psi}}{\partial t} = \mathcal{L}\Delta\boldsymbol{\Psi}, \tag{4}$$

where

$$\mathcal{L} = \begin{bmatrix} -2\psi_r\psi_i - 1 + \mathcal{D}_i + t_s\mathcal{D}_1 & -\psi_r^2 - 3\psi_i^2 + \alpha + \mathcal{D}_r \\ 3\psi_r^2 + \psi_i^2 - \alpha + \mathcal{D}_r & 2\psi_r\psi_i - 1 + \mathcal{D}_i + t_s\mathcal{D}_1 \end{bmatrix}, \tag{5}$$

and

$$\Delta\boldsymbol{\Psi} = \begin{bmatrix}\Delta\psi_i \\ \Delta\psi_r\end{bmatrix}. \tag{6}$$

The parameters $\mathcal{D}_r$ and $\mathcal{D}_i$ are the real and imaginary parts of $\mathcal{D}$, respectively, and $\mathcal{D}_1 = \mathcal{F}t^{-1}[D_1\mu]$ is the inverse Fourier transform of the group velocity term in the dispersion relation, where $D_1/2\pi$ is the FSR of the microresonator at the pumped mode.

The eigenvalues of $\mathcal{L}$ in Eq. (4) determine the stability of the initial soliton solution about which we perturb. If any of the eigenvalues are positive, the system is unstable; therefore, we check that all the eigenvalues are negative except for one eigenvalue that is fixed at the origin due to translational symmetry. From here, we systematically move through the $\alpha - F$ parameter space checking for stable solutions, which allows us to map out a region where stable solutions exist. As we vary α and F, the soliton solution eventually becomes unstable via a bifurcation that changes the solution; different bifurcation types lead to different outcomes. The outcome can be a new stationary solution, a breather, or some other type of evolving solution. More details on this process can be found in Ref. [39].

In our boundary tracking simulations, we estimated the parameters β, a, and b from stationary soliton solutions that we obtained through evolutionary simulations. To do so, we fixed the normalized detuning $\alpha = 10.04$, which corresponds to the experimental detuning $\delta = 1.5$ MHz for the spectrum in Fig. 2(a). We then varied β, a, and b to find the simulated soliton spectrum that matches the spectrum in Fig. 2(a) most closely. The resulting values were $\beta = -0.007$, $a = -10$, and $b = -25.3$. Figure 5(a) shows the experimental spectrum from Fig. 2(a) with the corresponding simulated spectrum with the chosen normalized parameters.

Figure 5(b) shows results with ($a = -10$) and without ($a = 0$) an avoided mode crossing for $b = -25.3$. The avoided crossing shifts the stable region toward higher pump detunings and powers. Additionally, a "bump" forms on the upper stability boundary near $\alpha = 6.5$. After this bump forms, a soliton-breather-soliton pattern can occur, as illustrated by the dashed black box in Fig. 5(b). In Figure 5(c) we show the different types of bifurcations and the corresponding solutions that occur as the stability boundary is crossed. In the dip after the bump on the upper boundary, solitons are unstable and breathers form. Moving from the dip back into the stable soliton region will result in the soliton reforming. Hence, as long as the chaotic region at lower detuning values is avoided, a soliton-breather-soliton pattern will appear in the α-F space as a solution trajectory enters, leaves, and then reenters the stable region via the top boundary of the stable region. We note that this pattern exists when $4.5 < F < 4.8$. When $F < 4.5$, we observe only a single soliton when increasing α after the system leaves the chaotic region. This result is consistent with our experimental observations.

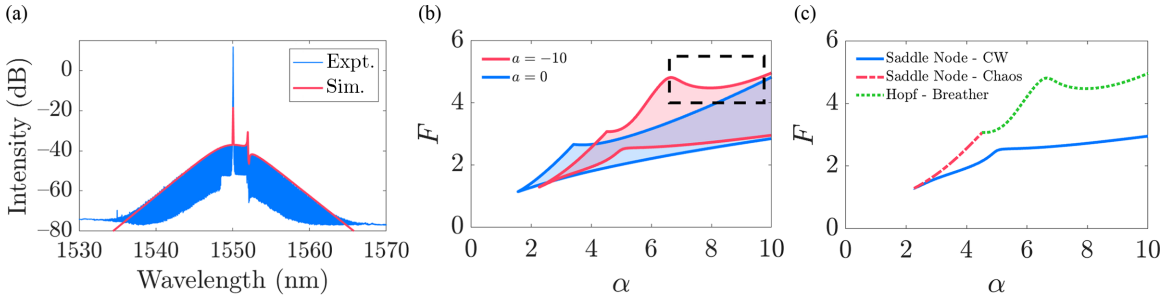

FIG. 5. (a) Comparison of experimental spectra from Fig. 2(a) and simulated single soliton spectra with parameters $\beta = -0.007$, $\alpha = 10.04$, $F = 3.91$, $a = -10$, and $b = -25.3$. (b) Stability boundary for $b = -25.3$ with $a = -10$ (red) and $a = 0$ (blue). The red (blue) shaded region indicates the region of stable single solitons. The dashed black box indicates the soliton-breather-soliton pattern location. (c) Stability boundary for $a = -10$ and $b = -25.3$ with different bifurcation types labeled.

IV. OVERLAID EXPERIMENTAL AND SIMULATION RESULTS FOR SINGLE SOLITONS AND BREATHERS

In Fig. 6 we overlay the experimental and simulated single soliton and intermode breather regions of existence. Figure 6 combines Fig. 4 and Fig. 5(b) by converting F and α (normalized power and detuning) to the experimental parameters P_{wg} and δ (pump power and detuning frequency, Fig. 4). These experimental parameters represent the power coupled into the coupling mechanism for the MgF_2 resonator (P_{wg}) and the effective detuning of the pump laser from the pumped resonance (δ). The conversions were done as follows.

To convert from α to δ, we use the normalizations in Ref. [41], which yields $\delta = \Omega - \omega_0$, where Ω is the pump's angular frequency and ω_0 is the pumped resonance's angular frequency. From there, we find $\alpha = 2\delta/\Delta\omega_0$, where $\Delta\omega_0 = \omega_0/Q_{\text{load}}$ and Q_{load} is the loaded microresonator cavity Q.

To convert from F to P_{wg}, we use the threshold power in the waveguide for the modulational instability (MI), P_{th}. In the normalized LLE given in Eq. (1), the normalized power F is defined such that $F^2 = 1$ is the threshold for MI [16], so that

$$\left(\frac{F}{1}\right)^2 = \frac{P_{\text{wg}}}{P_{\text{th}}}, \tag{7}$$

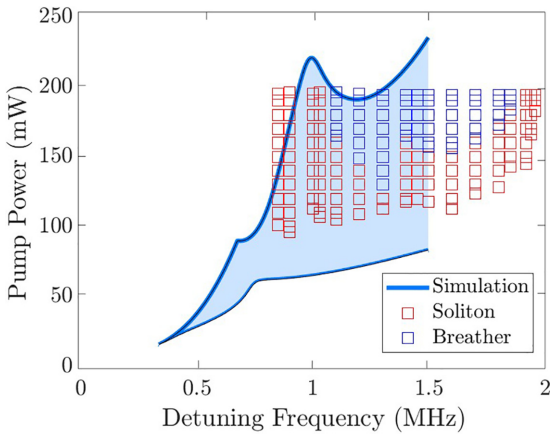

FIG. 6. Experimental vs simulation results for single solitons and breathers. The shaded area inside the simulation boundary is where single solitons are stable.

which implies $P_{\text{wg}} = P_{\text{th}}F^2$. We calculate P_{th} from the threshold formula in Ref. [42]:

$$P_{\text{th}} = \frac{\omega_0 A_{\text{eff}}}{4\eta n_2 D_1 Q_{\text{load}}^2}. \tag{8}$$

Table I presents the parameters that we used for our calculations. We experimentally measured the values of Q_{load} by making a transmission scan, and we calculated Q_{ext} and Q_{int} using the formula in Ref. [43]. We calculated A_{eff} using $A_{\text{eff}} = V_{\text{eff}}/L$, where V_{eff} is the effective mode volume, $L = 2\pi R$ is the microresonator optical path, and R is the microresonator radius. The values of V_{eff} and R were provided by OEWaves, the vendor of the MgF_2 microresonator that we used in our experiments. Using these values, we calculated $P_{\text{th,sim}} = 9.8$ mW. This value is in good agreement with our experimental MI threshold of $P_{\text{th,exp}} \approx 10$ mW.

From Fig. 6 we observe that although the calculated stability region is qualitatively accurate, there is some quantitative disagreement, and our computation only covers half the measured detuning range. However, given the simplified model of the avoided crossing that we are using in which it has an infinite slope and does not transfer energy to the second transverse mode family as does the model of [34], this model does reasonably well. This model greatly reduces the computational complexity required to simulate the system by only considering one set of longitudinal modes. This simplicity allows for the singularity model to be used in a wider variety of simulations without adding prohibitive run time costs.

TABLE I. Parameters used for the simulations. Parameter values with the source labeled as "This experiment" were either laser parameters (ω_0) measured during the experiment (D_1, Q) or calculated (η).

Parameter name	Value	Source
η	0.1395	This experiment
ω_0	1.215×10^{15} rad/s	This experiment
A_{eff}	3.2×10^{-10} m^2	From OEWaves
n_2	0.9×10^{-20} m^2/W	Material data
$D_1/2\pi$	$2\pi \times 9.9136 \times 10^9$ rad/s	This experiment
Q_{load}	6.47×10^8	This experiment
Q_{ext}	6.90×10^9	This experiment

This advantage was especially important for this study, which considered large values of α that required keeping a large number of discretized points in the azimuthal domain to accurately resolve the soliton solutions. Additionally, this model demonstrates that it is not necessary to invoke an energy transfer between transverse modes to explain the experimental observation of the soliton-breather-soliton transition.

V. CONCLUSION

In summary, we have experimentally explored single soliton and intermode breather soliton dynamics in a magnesium fluoride microresonator. We have investigated these regimes in the pump power–detuning (α-F) parameter space. We have identified a region in this space where an intermode breather soliton exists. With an input pump power above the soliton threshold, we find that as we change the detuning, we either obtain a single soliton or a continuous wave. However, at a higher input power, we enter a regime where as we detune, we first obtain a single soliton, then a soliton breather, and then a single soliton once again. To better understand our experimental results, we have numerically studied the stability of single solitons in the detuning–pump power parameter space by using a modified Lugiato-Lefever equation with an avoided mode crossing, where the avoided mode crossing only modifies the dispersion of the single transverse mode family that is being kept in our numerical model. The numerical results agree reasonably well with our experimental observations and show that the soliton-breather-soliton pattern can be induced by the presence of an avoided mode crossing while only considering one set of longitudinal modes.

ACKNOWLEDGMENTS

The authors gratefully acknowledge useful discussions with Pradyoth Shandilya. This paper is based upon work supported by, or in part by, the Army Research Laboratory and the Army Research Office under Contract or Grant No. W911NF2210131. Also, the work in this paper is partially supported by a project sponsored by the U.S. Department of Defense through Cooperative Agreement Award No. HQ0034-20-2-0007 under NCMS's Commercial Technologies for Maintenance Activities (CTMA) program. Project participants include the U.S. Army Combat Capabilities Development Command Army Research Laboratory, commonly referred to as DEVCOM ARL. In addition, this research was partially sponsored by the Air Force Office of Scientific Research and was accomplished under Grant No. W911NF-23-1-0166. The views and conclusions contained in this document are those of the authors and should not be interpreted as representing the official policies, either expressed or implied, of the Army Research Office or the U.S. Government. The U.S. Government is authorized to reproduce and distribute reprints for government purposes, notwithstanding any copyright notation herein.

DATA AVAILABILITY

The data used in this study is available from the corresponding author upon request.

[1] T. J. Kippenberg, R. Holzwarth, and S. A. Diddams, Microresonator-based optical frequency combs, Science **332**, 555 (2011).

[2] M.-G. Suh, Q.-F. Yang, K. Y. Yang, X. Yi, and K. J. Vahala, Microresonator soliton dual-comb spectroscopy, Science **354**, 600 (2016).

[3] W. Weng, E. Lucas, G. Lihachev, V. E. Lobanov, H. Guo, M. L. Gorodetsky, and T. J. Kippenberg, Spectral purification of microwave signals with disciplined dissipative Kerr solitons, Phys. Rev. Lett. **122**, 013902 (2019).

[4] D. T. Spencer *et al.*, An optical-frequency synthesizer using integrated photonics, Nature (London) **557**, 81 (2018).

[5] T. Herr, V. Brasch, J. D. Jost, C. Y. Wang, N. M. Kondratiev, M. L. Gorodetsky, and T. J. Kippenberg, Temporal solitons in optical microresonators, Nat. Photon. **8**, 145 (2014).

[6] H. Guo, M. Karpov, E. Lucas, A. Kordts, M. H. P. Pfeiffer, V. Brasch, G. Lihachev, V. E. Lobanov, M. L. Gorodetsky, and T. J. Kippenberg, Universal dynamics and deterministic switching of dissipative Kerr solitons in optical microresonators, Nat. Phys. **13**, 94 (2017).

[7] C. Joshi, J. K. Jang, K. Luke, X. Ji, S. A. Miller, A. Klenner, Y. Okawachi, M. Lipson, and A. L. Gaeta, Thermally controlled comb generation and soliton modelocking in microresonators, Opt. Lett. **41**, 2565 (2016).

[8] Q. Li, T. C. Briles, D. A. Westly, T. E. Drake, J. R. Stone, B. R. Ilic, S. A. Diddams, S. B. Papp, and K. Srinivasan, Stably accessing octave-spanning microresonator frequency combs in the soliton regime, Optica **4**, 193 (2017).

[9] S. Zhang, J. M. Silver, L. D. Bino, F. Copie, M. T. M. Woodley, G. N. Ghalanos, A. Ø. Svela, N. Moroney, and P. Del'Haye, Sub-milliwatt-level microresonator solitons with extended access range using an auxiliary laser, Optica **6**, 206 (2019).

[10] Z. Qi, A. Leshem, J. A. Jaramillo-Villegas, G. D'Aguanno, T. F. Carruthers, O. Gat, A. M. Weiner, and C. R. Menyuk, Deterministic access of broadband frequency combs in microresonators using cnoidal waves in the soliton crystal limit, Opt. Express **28**, 36304 (2020).

[11] Z. Kang, F. Li, J. Yuan, K. Nakkeeran, J. N. Kutz, Q. Wu, C. Yu, and P. K. A. Wai, Deterministic generation of single soliton Kerr frequency comb in microresonators by a single shot pulsed trigger, Opt. Express **26**, 18563 (2018).

[12] J. Li, S. Wan, J.-L. Peng, Z.-Y. Wang, R. Niu, C.-L. Zou, G.-C. Guo, and C.-H. Dong, Thermal tuning of mode crossing and the perfect soliton crystal in a Si_3N_4 microresonator, Opt. Express **30**, 13690 (2022).

[13] Y. K. Chembo, D. V. Strekalov, and N. Yu, Spectrum and dynamics of optical frequency combs generated with monolithic whispering gallery mode resonators, Phys. Rev. Lett. **104**, 103902 (2010).

[14] Y. K. Chembo and N. Yu, Modal expansion approach to optical-frequency-comb generation with monolithic

whispering-gallery-mode resonators, Phys. Rev. A **82**, 033801 (2010).
[15] X. Wang, W.-q. Wang, P. Xie, Y. Wang, S. T. Chu, B. Little, W. Zhao, and W.-f. Zhang, Avoided mode-crossing assisted single soliton formation, Opt. Laser Technol. **161**, 109118 (2023).
[16] C. Godey, I. V. Balakireva, A. Coillet, and Y. K. Chembo, Stability analysis of the spatiotemporal Lugiato-Lefever model for Kerr optical frequency combs in the anomalous and normal dispersion regimes, Phys. Rev. A **89**, 063814 (2014).
[17] P. Parra-Rivas, D. Gomila, M. A. Matías, S. Coen, and L. Gelens, Dynamics of localized and patterned structures in the Lugiato-Lefever equation determine the stability and shape of optical frequency combs, Phys. Rev. A **89**, 043813 (2014).
[18] J. A. Jaramillo-Villegas, X. Xue, P.-H. Wang, D. E. Leaird, and A. M. Weiner, Deterministic single soliton generation and compression in microring resonators avoiding the chaotic region, Opt. Express **23**, 9618 (2015).
[19] E. Lucas, M. Karpov, H. Guo, M. L. Gorodetsky, and T. J. Kippenberg, Breathing dissipative solitons in optical microresonators, Nat. Commun. **8**, 736 (2017).
[20] M. Karpov, M. H. P. Pfeiffer, H. Guo, W. Weng, J. Liu, and T. J. Kippenberg, Dynamics of soliton crystals in optical microresonators, Nat. Phys. **15**, 1071 (2019).
[21] H. Zhang, L. Lu, J. Chen, and L. Zhou, Program-controlled single soliton generation driven by the thermal-compensated avoided mode crossing, J. Lightwave Technol. **41**, 1801 (2023).
[22] H. Liu, W. Wang, J. Yang, M. Yu, D.-L. Kwong, and C. W. Wong, Observation of deterministic double dissipative-Kerr-soliton generation with avoided mode crossing, Phys. Rev. Res. **5**, 013172 (2023).
[23] C. Bao, J. A. Jaramillo-Villegas, Y. Xuan, D. E. Leaird, M. Qi, and A. M. Weiner, Observation of Fermi-Pasta-Ulam recurrence induced by breather solitons in an optical microresonator, Phys. Rev. Lett. **117**, 163901 (2016).
[24] M. Yu, J. K. Jang, Y. Okawachi, A. G. Griffith, K. Luke, S. A. Miller, X. Ji, M. Lipson, and A. L. Gaeta, Breather soliton dynamics in microresonators, Nat. Commun. **8**, 14569 (2017).
[25] S. Wan, R. Niu, Z.-Y. Wang, J.-L. Peng, M. Li, J. Li, G.-C. Guo, C.-L. Zou, and C.-H. Dong, Frequency stabilization and tuning of breathing solitons in Si_3N_4 microresonators, Photon. Res. **8**, 1342 (2020).
[26] D. C. Cole, E. S. Lamb, P. Del'Haye, S. A. Diddams, and S. B. Papp, Soliton crystals in Kerr resonators, Nat. Photon. **11**, 671 (2017).
[27] Z. Qi, S. Wang, J. Jaramillo-Villegas, M. Qi, A. M. Weiner, G. D'Aguanno, T. F. Carruthers, and C. R. Menyuk, Dissipative cnoidal waves (Turing rolls) and the soliton limit in microring resonators, Optica **6**, 1220 (2019).
[28] Z. Lu, H.-J. Chen, W. Wang, L. Yao, Y. Wang, Y. Yu, B. E. Little, S. T. Chu, Q. Gong, W. Zhao, X. Yi, Y.-F. Xiao, and W. Zhang, Synthesized soliton crystals, Nat. Commun. **12**, 3179 (2021).
[29] C. E. Murray, M. Tan, C. Prayoonyong, X. Zhu, S. T. Chu, B. E. Little, R. Morandotti, A. Mitchell, D. J. Moss, and B. Corcoran, Investigating the thermal robustness of soliton crystal microcombs, Opt. Express **31**, 37749 (2023).
[30] T. Carmon, L. Yang, and K. J. Vahala, Dynamical thermal behavior and thermal self-stability of microcavities, Opt. Express **12**, 4742 (2004).
[31] V. Brasch, M. Geiselmann, M. H. P. Pfeiffer, and T. J. Kippenberg, Bringing short-lived dissipative Kerr soliton states in microresonators into a steady state, Opt. Express **24**, 29312 (2016).
[32] D. C. Cole, J. R. Stone, M. Erkintalo, K. Y. Yang, X. Yi, K. J. Vahala, and S. B. Papp, Kerr-microresonator solitons from a chirped background, Optica **5**, 1304 (2018).
[33] C. Bao, Y. Xuan, D. E. Leaird, S. Wabnitz, M. Qi, and A. M. Weiner, Spatial mode-interaction induced single soliton generation in microresonators, Optica **4**, 1011 (2017).
[34] H. Guo, E. Lucas, M. H. P. Pfeiffer, M. Karpov, M. Anderson, J. Liu, M. Geiselmann, J. D. Jost, and T. J. Kippenberg, Intermode breather solitons in optical microresonators, Phys. Rev. X **7**, 041055 (2017).
[35] E. Lucas, H. Guo, J. D. Jost, M. Karpov, and T. J. Kippenberg, Detuning-dependent properties and dispersion-induced instabilities of temporal dissipative Kerr solitons in optical microresonators, Phys. Rev. A **95**, 043822 (2017).
[36] Y. Chen, T. Liu, S. Sun, and H. Guo, Temporal dissipative structures in optical Kerr resonators with transient loss fluctuation, Opt. Express **29**, 35776 (2021).
[37] P. Del'Haye, O. Arcizet, M. L. Gorodetsky, R. Holzwarth, and T. J. Kippenberg, Frequency comb assisted diode laser spectroscopy for measurement of microcavity dispersion, Nat. Photon. **3**, 529 (2009).
[38] S. Wang, A. Docherty, B. S. Marks, and C. R. Menyuk, Boundary tracking algorithms for determining the stability of mode-locked pulses, J. Opt. Soc. Am. B **31**, 2914 (2014).
[39] Edited by L. Courtright, Z. Qi, T. F. Carruthers, and C. R.Menyuk, in *Automatically Mapping the Stable Regions of Frequency Combs in Microresonators* (Optica Publishing Group, Washington, DC, 2021).
[40] T. Herr, V. Brasch, J. D. Jost, I. Mirgorodskiy, G. Lihachev, M. L. Gorodetsky, and T. J. Kippenberg, Mode spectrum and temporal soliton formation in optical microresonators, Phys. Rev. Lett. **113**, 123901 (2014).
[41] Y. K. Chembo and C. R. Menyuk, Spatiotemporal Lugiato-Lefever formalism for Kerr-comb generation in whispering-gallery-mode resonators, Phys. Rev. A **87**, 053852 (2013).
[42] J. Li, H. Lee, T. Chen, and K. J. Vahala, Low-pump-power, low-phase-noise, and microwave to millimeter-wave repetition rate operation in microcombs, Phys. Rev. Lett. **109**, 233901 (2012).
[43] Y. Zhang, K. Zhong, G. Hu, D. Yi, R. R. Kumar, and H. K. Tsang, Sub-milliwatt optical frequency combs in dual-pumped high-Q multimode silicon resonators, Appl. Phys. Lett. **117**, 221103 (2020).